frontiers | Frontiers in Earth Science

TYPE Original Research
PUBLISHED 24 March 2025
DOI 10.3389/feart.2025.1566088

OPEN ACCESS

EDITED BY
Claudia Belviso,
National Research Council (CNR), Italy

REVIEWED BY
Xin Chen,
China University of Geosciences Wuhan, China
Lianjie Zhao,
Shandong University of Technology, China
Wenbo Sun,
Central South University, China

*CORRESPONDENCE
Hongjie Shen,
shenhongjie0627@qq.com

RECEIVED 24 January 2025
ACCEPTED 10 March 2025
PUBLISHED 24 March 2025

CITATION
Peng N, Shen H and Liao J (2025) Quartz textural and trace-element geochemical constraints on the origin of lode gold deposits: a case study of the Yanzhupo deposit in Jiangnan Orogen (South China). *Front. Earth Sci.* 13:1566088.
doi: 10.3389/feart.2025.1566088

Quartz textural and trace-element geochemical constraints on the origin of lode gold deposits: a case study of the Yanzhupo deposit in Jiangnan Orogen (South China)

Nengli Peng[1], Hongjie Shen[2,3]* and Jia Liao[1]

[1]Changsha General Survey of Natural Resources Center, China Geological Survey, Changsha, China, [2]Key Laboratory of Metallogenic Prediction of Nonferrous Metals and Geological Environment Monitor (Central South University), Ministry of Education, Changsha, China, [3]School of Geosciences and Info-Physics, Central South University, Changsha, China

The Jiangnan Orogen (South China) is endowed with many important gold deposits, whose genesis remains controversial. The Yanzhupo is a representative gold deposit (2.50 t Au @ 2.52 g/t) in the Jiangnan Orogen, characterized by multi-stage quartz formation. Its mineralization can be divided into three stages (I) quartz-ankerite-pyrite (II) quartz-ankerite-chlorite-pyrite-gold, and (III) quartz-ankerite-calcite-pyrite. Multiple generations of quartz were identified at Yanzhupo. Stage I quartz (Qz1) commonly coexists with pyrite and is coarse-grained, and texturally homogeneous. Stage II quartz (Qz2) is divided into two generations, namely, Qz2a and Qz2b, and the homogeneous Qz2a is often replaced by the veined/stockwork Qz2b. Stage III quartz (Qz3) comprises two generations of quartz, namely, the earlier, texturally homogeneous Qz3a, and the younger Qz3b that replaced Qz3a. Qz1 is Ti-rich (median: 0.743 ppm) and Al-depleted (median: 294 ppm), indicating that it was formed at high temperatures and pH levels. The ensuing drop in temperature and pH favored the formation of Qz2a. However, the abrupt decrease in Al concentration from Qz2a (median: 1,383 ppm) to Qz2b (median: 120 ppm) suggests that it was created at a high pH, which might have been caused by an intense water-rock interaction, resulting in Stage II Au precipitation. Finally, the sealing of fractures by veins may have resulted in the production of Qz3 in stable settings, evidenced by the As-rich and Ti-depleted Qz3 than Qz2b. The Yanzhupo Au deposit has Al and Ti contents and Al/Ti ratios that are similar to those found in magmatic-hydrothermal deposits, implying that it is likely of magmatic-hydrothermal origin. These findings show that the coupled examination of quartz texture and geochemistry can provide important clues to the mineralization history, origin of gold deposits, and the distribution characteristics of gold mineralization, and give vital insights into the origin of Au mineralization in the Jiangnan Orogen (South China).

KEYWORDS

quartz, trace element geochemistry, Yanzhupo Au deposit, Jiangnan Orogen, magmatic-hydrothermal origin

1 Introduction

Quartz, a typical mineral in many hydrothermal environments (Rusk et al., 2008), is extremely resistant to change and keeps a continuous geochemical record of trace elements that may be utilized to reconstruct the history of mineral creation (Rusk 2012; Müller et al., 2018; Hong et al., 2024). Several generations of quartz with various micro-textures may be distinguished using cathodoluminescence (CL) images, which provide information on hydrothermal development (Rusk et al., 2008; Wertich et al., 2018; Qiu et al., 2021; Yuan et al., 2023). Temperature, oxygen fugacity (fO_2), pH, growth rate, and fluid composition are the main factors that influence the incorporation of trace elements into quartz (Rusk et al., 2008; Tanner et al., 2013; Müller et al., 2018). Accordingly, the texture and trace element compositions of quartz as assessed by CL can offer important insights into the origin of the ore and the intricate ore process of hydrothermal systems (Hong et al., 2024; Gao et al., 2022; Qiu et al., 2022). The structure and geochemistry of quartz have been successfully used in a variety of hydrothermal deposits, especially in porphyry deposits (Müller et al., 2010; Hong et al., 2024) and skarn (Zhang Y. et al., 2019). The genesis of unknown deposits can be ascertained using this categorization as a basis.

The Neoproterozoic Yangtze–Cathaysia Block continent-continent collision along the Shaoxing–Jiangshan–Piangxiang–Shuangpai fault zone created the Jiangnan Orogen in the South China Block (Figure 1A) (Yan et al., 2015). With a total gold resource of around 950 t, the orogen is one of South China's major gold producers (Deng et al., 2017; 2020). Even though there have been a lot of studies on regional gold mineralization, several metallogenic models have been proposed because of the multiphase orogenic activities, the close spatial-temporal relationship between granite and gold mineralization, the complexity of the ore-forming fluids, and the source of materials, including orogenic-type (Zhao et al., 2013; Xu D. et al., 2017; Liu et al., 2019), sedimentary exhalative (SEDEX)-type (Gu et al., 2007; Gu et al., 2012), intrusion-related (Jia et al., 2019; Li et al., 2019; Feng et al., 2020a; Feng et al., 2020b; Li et al., 2021), epithermal (Ye et al., 1994), and intracontinental reactivation-type model (Deng et al., 2017; Xu D. R. et al., 2017).

Situated in the center of the Jiangnan Orogen, the Yanzhupo gold deposit has a confirmed ore resource of 2.50 t Au @ 2.52 g/t (China Geological Survey, 2024). It is a prime candidate for using quartz geochemistry to restrict the mineralization history due to its widespread occurrence of muti-generations of quartz. This work employs laser ablation inductively coupled plasma-mass spectrometry (LA–ICP–MS) in conjunction with scanning electron microscope cathodoluminescence (SEM-CL) imaging to investigate the trace-element geochemistry of the Yanzhupo multistage quartz. Our goals are to clarify the physicochemical circumstances and history of ore formation, disentangle the ore-forming process, and offer fresh insights into the Jiangnan Orogen's Au mineralization origin.

2 Geological setting

2.1 Regional geology

After the Paleo-South China Ocean closed and the blocks collided between 980 and 820 Ma, the Neoproterozoic assembly of the Yangtze and Cathaysia Block created the NE-NEE trending Jiangnan orogen in South China (Figure 1A) (Cawood et al., 2013; Yao et al., 2019; Shu et al., 2021). The Neoproterozoic collisional event was accompanied by two magmatic events: the emplacement of bimodal igneous rocks between 780 and 730 Ma and massive granitic plutons between 835 and 800 Ma (Li et al., 2003; Li et al., 2005). Stable sedimentation followed post-orogenic expansion in the late Neoproterozoic (Wang and Shu, 2012). Numerous gold occurrences in this area are wallrocks made of these Neoproterozoic metamorphosed sedimentary rocks (Li et al., 2021). In the early Paleozoic, the Yangtze and Cathaysian Blocks once more came together and collided (Faure et al., 2009). The early Paleozoic tectonic event is identified by the intrusion of S-type granites and migmatites from the late Silurian to the Early Devonian, unconformably overlain by Devonian successions (Chu et al., 2012; Xu D. et al., 2017). Many folds and nappe faults were created in the orogen as a result of the early Mesozoic collision between South China and North China (Wang et al., 2005). The basin-ridge structure was first created in the late Mesozoic with the transition from the Tethys Ocean to the ancient Pacific plate (Zhang et al., 2012). With a total gold resource of approximately 970 t, the Jiangnan orogen may have produced numerous gold-polymetallic deposits due to complex and protracted orogenic movement, 40 of which are dispersed along the deep faults that trend NE-NNE (Wang et al., 2014; Li et al., 2016; Zhang L. et al., 2019).

Tectonically situated in the middle Jiangnan Orogen, northeastern Hunan (NE Hunan) is also regarded as a portion of the late Mesozoic South China Basin-and-Range Province (Figure 1). The most significant gold district in the Jiangnan Orogen is NE Hunan (gold reserve >315 t) (Zhang L. et al., 2019; Xiong et al., 2020; Zhou et al., 2021). It is home to numerous giant-large gold deposits, such as the Wangu (85 t Au @ 6.8 g/t; Wen et al., 2016), Huangjindong (~80 t Au @ 4.0–10.0 g/t; Han et al., 2010), and Zhengchong (116 t Au @ 3.2 g/t; Liu et al., 2019). The Neoproterozoic Lengjiaxi group of low-grade metamorphosed turbidites, Cambrian-nanhua System sandstone, limestone and shale, and Quaternary-Cretaceous sandstone and conglomerate dominate the exposed strata in northeastern Hunan (Li et al., 2020; Li et al., 2022; Madayipu et al., 2024). From the Neoproterozoic to the Mesozoic, many intrusive activity events were recorded in northeastern Hunan (Figure 1B) (Xu D. et al., 2017; Wang et al., 2020a; 2020b; Madayipu et al., 2023a; Madayipu et al., 2023b). The Changsanbei granodiorite (zircon U–Pb age: 845 ± 4 Ma; Deng et al., 2020) and Hongxiaqiao biotite granodiorite and Banshanpu biotite monzogranite (zircon U–Pb age: 423–421 Ma; Li et al., 2015) respectively reflect the Neoproterozoic and early Paleozoic intrusion. The most common and distinctively S-type granites are those of the Late Mesozoic, such as the Mufushan biotite monzogranite (zircon U–Pb age: 158–125 Ma; Wang et al., 2014; Xiong et al., 2020) and the Lianyunshan two-mica monzogranite (zircon U–Pb age: 150–140 Ma; Wang et al., 2016; Xu D. R. et al., 2017). The three ductile-shear zones (Cili–Linxiang, Xiaochijie–Lianyunshan, and Anhua–Liuyang ductile-shear zones) and Basin-and-Range-like topography are the key regional features in the NE Hunan district (Han et al., 2010; Xu D. et al., 2017; Zhou et al., 2019). The predominately NE-to NNE-trending faults cut or reactivate a variety of E-W-, NE-, and NW-trending faults

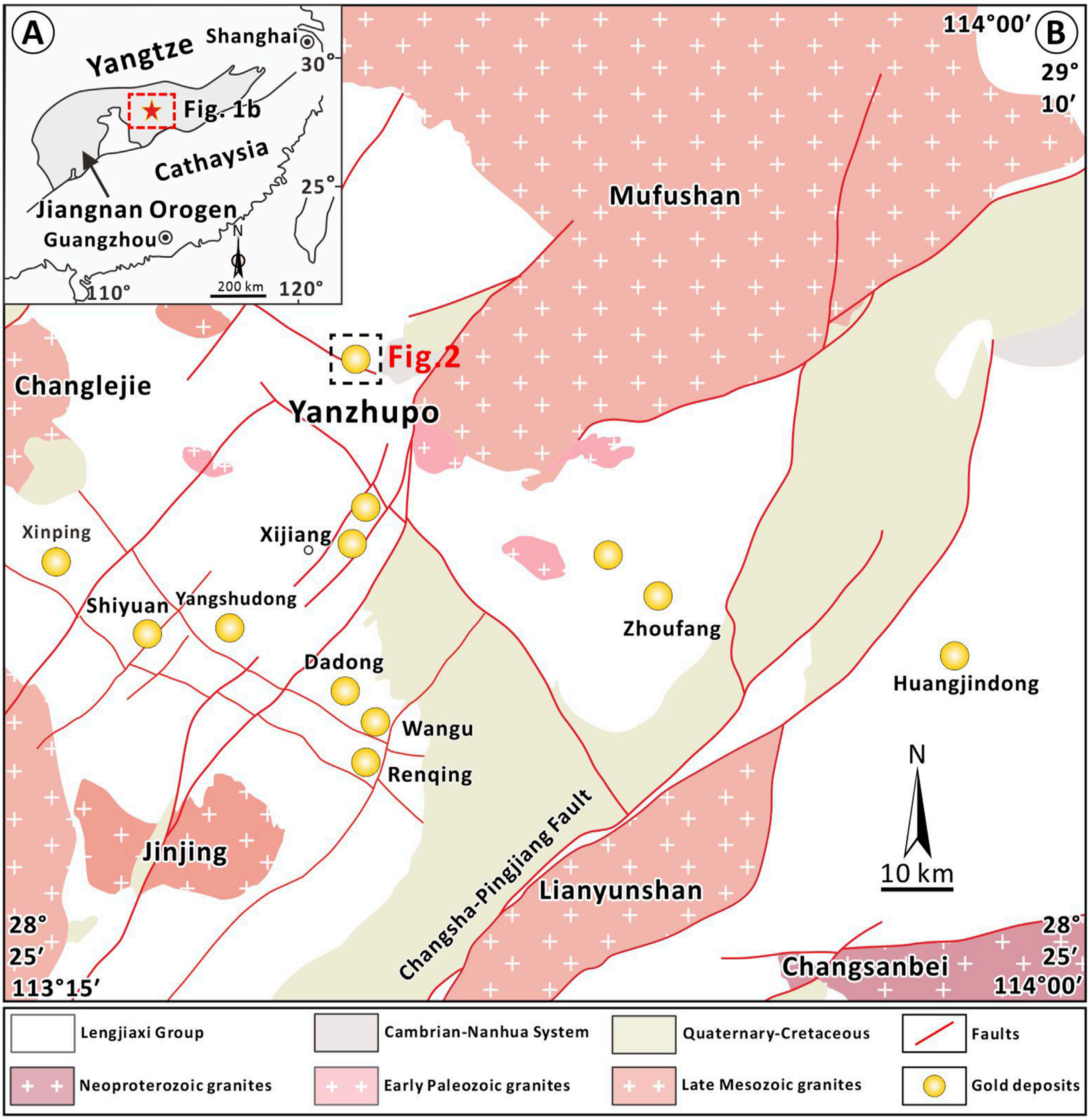

FIGURE 1
(A) Location of Jiangnan Orogen (Ji et al., 2018); **(B)** Geologic map of northeastern Hunan Province (Lu et al., 2020; Wang et al., 2024).

that were developed in the early phase. The regional NNE-trending faults, which imposed first-order structural control, are where the gold resources are spatially concentrated. Nonetheless, the majority of the gold mineralization is found in second or third-order faults, such as those that trend NW and NNE (Tan et al., 2022).

2.2 Deposit geology

The Yanzhupo deposit is located in Pingjiang County, northeastern Hunan (Figure 2A). The Neoproterozoic Lengjiaxi Group, which includes the Huanghudong Formation, Leishenmiao Formation, and Panjiacong Formation, makes up the majority of the relatively basic local outcropping sequences in the deposit. The strata mainly trend northwest. The distribution of the Quaternary system is primarily banded. The Cambrian Fulu Formation, which is angularly unconformable above the Lengjiaxi Group strata and mostly consists of a series of gray-green medium-thick bedded conglomerate or conglomerate sandstone, is exposed in modest amounts in the eastern and northwest portions of the Yanzhupo deposit. The main host of gold ore in the region is the sandstone slate of the Leishenmiao Formation in the Lengjiaxi Group (Figure 2B).

Local stratigraphic inversion results from small-scale folds, which are the predominant fold types in the region. Mostly found

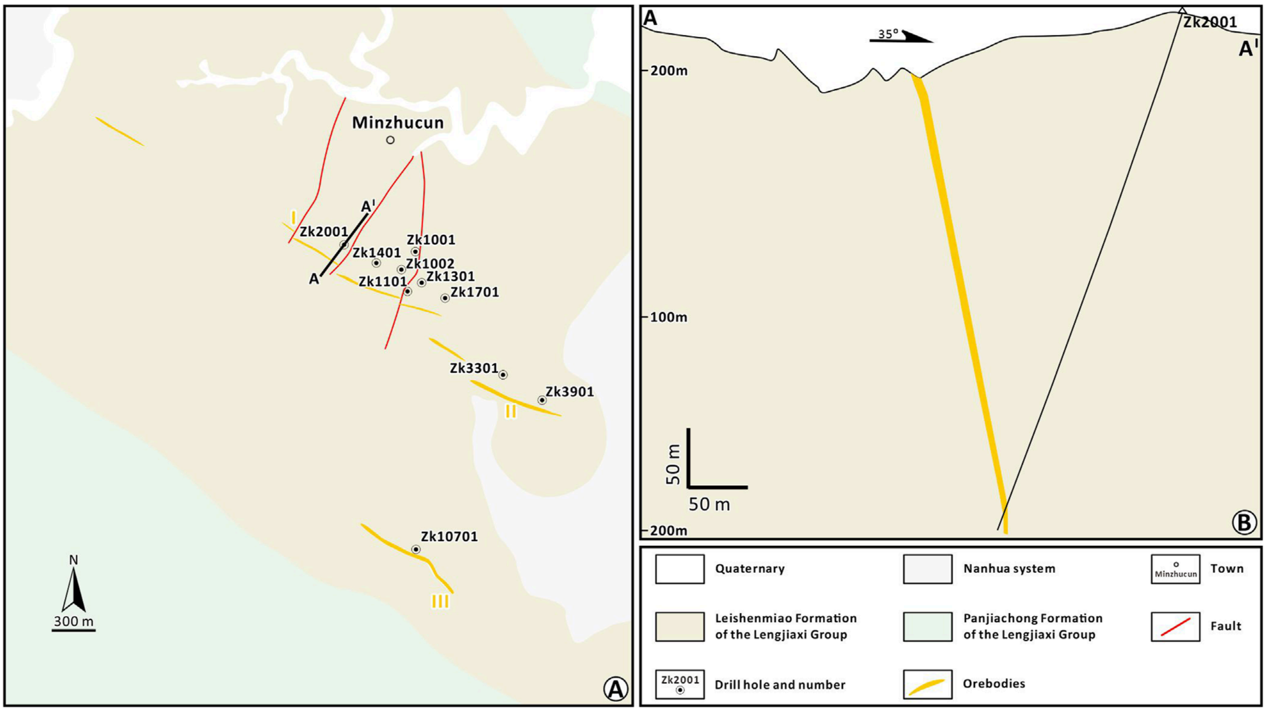

FIGURE 2
(A) Geologic map and **(B)** typical geological profile of the Yanzhupo Au deposit.

in the northern and western regions, the fault structures are comparatively well-developed and oriented mostly in the northeast and northwest (west) directions, while there are also east-west faults. The most important main ore-controlling and ore-conducting structures in the deposit are the northwest (west) oriented faults, which dip NE with a few small dips to the south at 45°–60°. Tectonic breccia, shattered rock, mylonitic slate, and quartz veins make up the majority of the fault fracture zones. Pyrite alteration can be found locally in the tectonic breccia and shattered rock. Additionally, no outcrops of igneous rocks were observed in the deposit.

At Yanzhupo, three distinct gold ore veins have been identified (China Geological Survey, 2024). With a dip angle of 60°–80°, the No. I vein strikes northwest and dips northeast. The gold grade ranges from 0.12 to 8.38 g/t, the mineralized zone width is 0.35–3.85 m, and the surface-controlled length is 1,250 m. The vein is mostly composed of quartz veins scattered across broken altered slate. With very slight variations in thickness and strong mineralization continuity, the vein stretches along its strike and dips somewhat steadily. One distinct orebody, designated I-1, has a dip angle of 70°, strikes NW, and dips NE. With an initial estimated gold resource of 1.25 t, the controlled length is 400 m, the controlled inclination depth is 330 m, the average thickness is 1.52 m, and the average grade is 2.52 g/t. The No. II vein has a dip angle of 60°–70°, striking NW and dipping NE. The gold grade ranges from 0.19 to 40.70 g/t, the mineralized zone width is 0.36–1.56 m, and the surface-controlled length is 1,200 m. The vein is primarily composed of quartz veins scattered throughout broken altered slate. With a dip angle of 60°–80°, the No. III vein strikes northwest and dips northeast. The gold grade ranges from 0.20 to 6.13 g/t, the mineralized zone width is 0.25–0.97 m, and the surface-controlled length is 560 m. Quartz veins make up the majority of the veins. Deep mineralization has weakened, and the mineralization is inconsistent.

3 Paragenetic sequence of mineralization and alteration

Three stages of the mineralization/alteration paragenetic sequence at Yanzhupo can be distinguished based on the mineral assemblages and textural relationships (I) Quartz-ankerite-pyrite (II) Quartz-ankerite-chlorite-pyrite-native gold, and (III) Quartz-ankerite-calcite-pyrite (Figure 3).

Stage I is dominated by a significant proportion of quartz and ankerite, a little amount of pyrite and chalcopyrite, and trace quantities of galena (Figures 4A–C), occurring mainly as veins (0.8–1.0 cm wide; Figures 4A, D, E). The subhedral to anhedral porous pyrite (0.3 mm–2 cm; Figures 4B, C) with galena and chalcopyrite inclusions in the quartz-ankerite-pyrite vein is linked to significant silicification (China Geological Survey, 2024). Chalcopyrite, which is subhedral-anhedral (Figures 4B, C), is mostly found inside the quartz-ankerite-pyrite vein and along the margin of pyrite.

The Stage I quartz-ankerite-pyrite veins (usually 0.8–1.0 cm wide) are frequently intersected by Stage II quartz-ankerite-chlorite-pyrite-native gold veins (4.0–5.0 cm wide) (Figure 4D). Furthermore, significant silicification and pyrite alteration are also linked to Stage II (China Geological Survey, 2024). With grain sizes ranging from 20 to 500 μm, pyrite is usually subhedral to

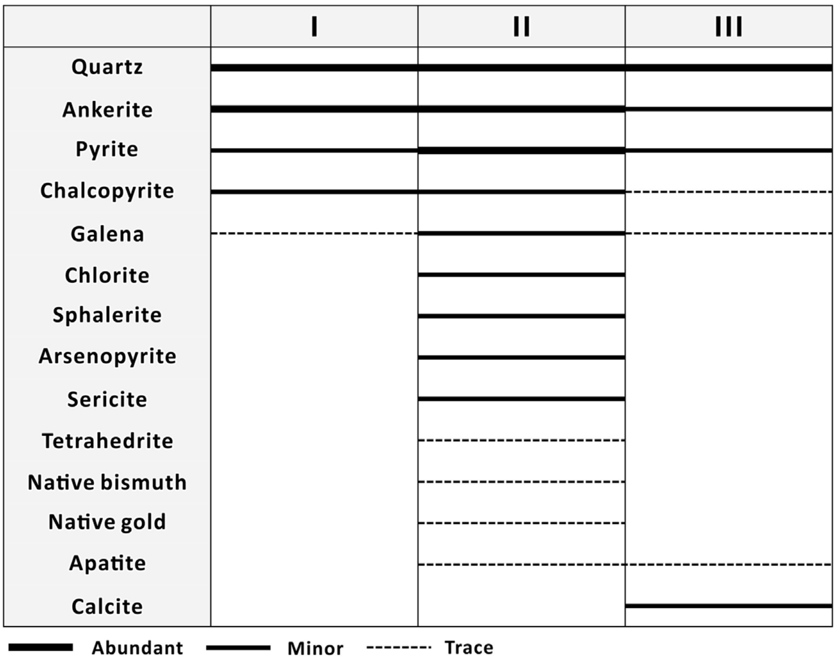

FIGURE 3
Alteration and mineralization paragenetic sequence at Yanzhupo.

anhedral and mostly appears in irregular lumps or tiny vein formations inside veins (Figure 4F). Pyrite has well-developed fractures that are frequently filled with sphalerite, tetrahedrite, galena, and chalcopyrite (Figure 4F). With grain sizes ranging from 20 μm to 1 mm, subhedral to anhedral arsenopyrite is found in the veins and wall rock. Arsenopyrite and native gold are closely related (Figure 4G). A tiny quantity of anhedral chalcopyrite, galena, sphalerite, and tetrahedrite is encased in pyrite, but the majority are found inside the veins (Figure 4H). Furthermore, previous study demonstrates that sporadic fine-grained tabular rutile (Ti-rich) and anhedral apatite can be observed in the quartz veins of Stage II (Liao et al., 2025).

It is usual for Stage I quartz-ankerite-pyrite veins (Figures 4D,E) and Stage II quartz-ankerite-chlorite-pyrite-native gold veins (Figure 4I) to be cut by Stage III quartz-ankerite-calcite-pyrite veins (0.5–1.0 cm wide; Figure 4I). The primary processes linked to this stage are silicification and carbonation (China Geological Survey, 2024). Coexisting with quartz, ankerite, and calcite, pyrite is subhedral-anhedral, fragmented, and has a particle size of 0.1–1.0 mm (Figure 4J). Additionally, the pyrite fractures and the quartz-carbonate veins include anhedral galena and chalcopyrite.

4 Sampling and analytical methods

4.1 Samples

Thirty-nine samples were taken from drill cores. Twelve samples of quartz-rich ore were chosen for textural and geochemical analyses. Detailed sample descriptions are listed in Table 1. These samples were thus chosen for petrographic examination using cathodoluminescence (CL) imaging and reflected and transmitted polarized light microscopy. Five were then selected for LA–ICP–MS trace element spot analysis (ZK3502-13, ZK3502-40, ZK3502-44, ZK3502-44, ZK1002-36).

4.2 Scanning electron microscope cathodoluminescence (SEM-CL) imaging

In order to study the interior texture of the quartz before trace element analysis, the quartz crystals in these six samples were imaged using scanning electron microscope cathodoluminescence (SEM-CL) before the LA–ICP–MS analysis. A TESCAN MIRA4 field-emission scanning electron microscope (FE-SEM) was used at Weitan Technology Co. Ltd. in Changsha, China, to perform quartz cathodoluminescence (CL) imaging. An accelerating voltage of 8 keV and a beam current of 1 nA were the parameters used for CL imaging.

4.3 LA–ICP–MS quartz trace element analysis

Femtosecond laser-ablation inductively coupled plasma-mass spectrometry (fs–LA–ICP–MS) was utilized to analyze the trace elements in quartz. The analyses were conducted at Chemlabpro Technology Co. Ltd. (Shanghai, China). A Genesis GEO model femtosecond laser ablation system was used in conjunction with an Agilent 8,900 triple quadrupole ICP–MS. The carrier gas used in the experiment is 99.999% pure helium, flowing at a rate of 600 mL per minute. A 50 μm spot size, an energy density of 5 J/cm^2, a laser repetition rate of 2 Hz, and a 45 s ablation duration were used for the laser ablation analysis. Each ablation area was preceded

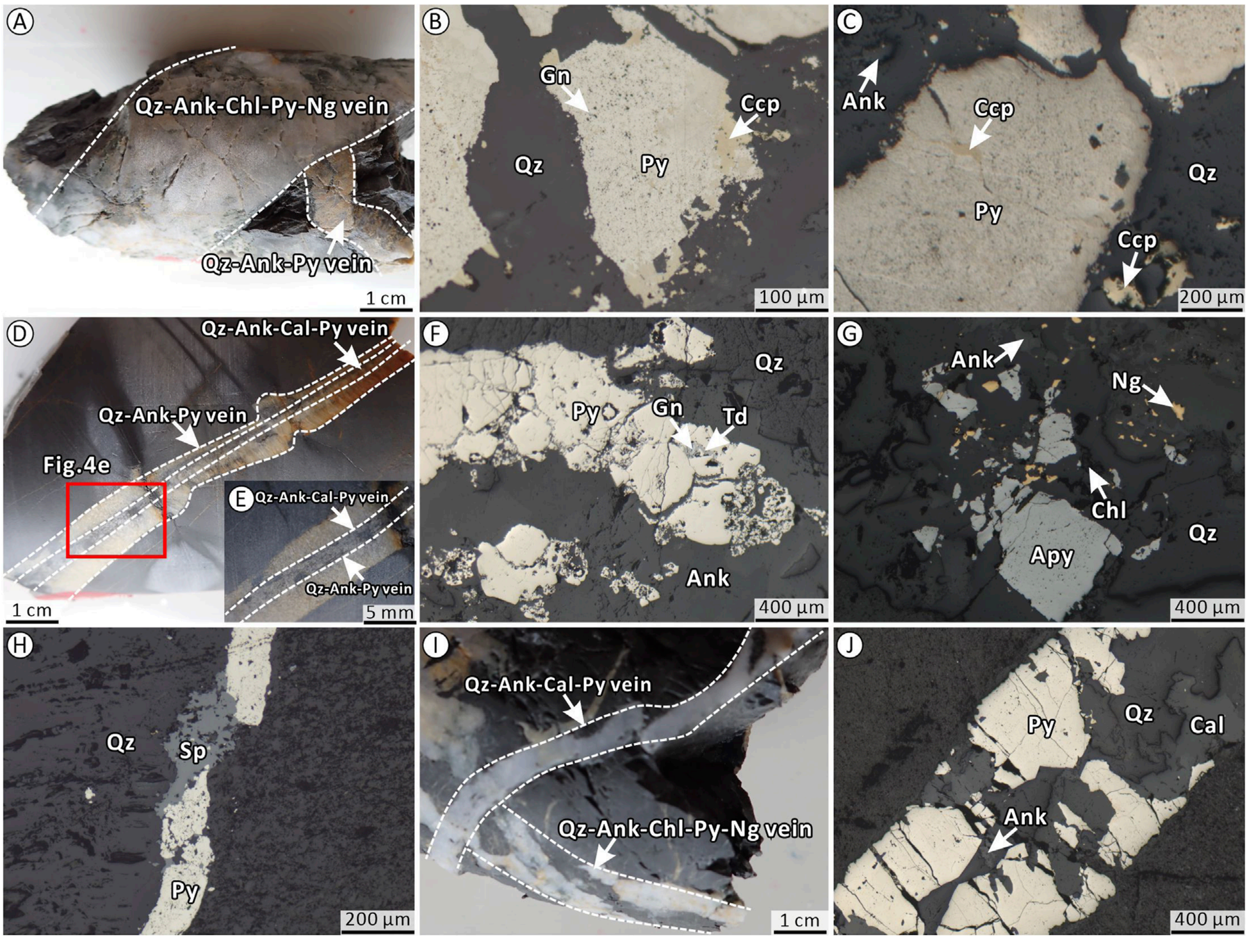

FIGURE 4
Typical alteration and mineralization photos at Yanzhupo: **(A)** Stage I quartz-ankerite-pyrite veins cut by Stage II quartz-ankerite-chlorite-pyrite-native gold veins; **(B)** Pyrite with galena and chalcopyrite inclusions in the quartz-ankerite-pyrite vein; **(C)** Chalcopyrite found inside the quartz-ankerite-pyrite vein and along the margin of pyrite; **(D, E)** Stage II quartz-ankerite-chlorite-pyrite-native gold veins cut Stage I quartz-ankerite-pyrite veins; **(F)** Pyrite often has well-developed fractures filled with sphalerite, tetrahedrite, galena, and chalcopyrite; **(G)** Arsenopyrite closely associated with native gold; **(H)** Chalcopyrite, galena, sphalerite, and tetrahedrite encased in pyrite; **(I)** Stage I quartz-ankerite-pyrite veins and Stage II quartz-ankerite-chlorite-pyrite-native gold veins cut by Stage III quartz-ankerite-calcite-pyrite veins; **(J)** Pyrite coexist with quartz, ankerite, and calcite. Abbreviations: Py, pyrite; Sp, sphalerite; Gn, galena; Apy, arsenopyrite; Ccp, chalcopyrite; Td, tetrahedrite; Ng, native gold; Qz, quartz; Cal, calcite; Ank, ankerite; Chl, chlorite.

and followed by a 25 s warm-up and washout time. The elements that are measured include As, Rb, Sr, Zr, Nb, Sn, Sb, Cs, Nd, Gd, Hf, Pb, Li, Na, Mg, Al, Si, P, K, Ca, Ti, V, Cr, Mn, Fe, Cu, Zn, Ge, and As. External standards were the international standard reference materials ARM-3, NIST616, NIST614, and NIST612. Standards were examined at 10-point intervals. With a sample depth of 7.0 mm and a nebulizer gas flow rate of 850 mL/min, the ICP-MS ran at 1550 W. The entire mass spectrometry collection time was around 80 s, with each single-element scan taking 0.03 s and the scan cycle for all elements lasting 1.0426 s Iolite4 software was used to treat the experimental data utilizing a multi-external standard normalization procedure.

5 Results

5.1 Generations characteristics of quartz

Quartz from the Yanzhupo gold deposit into five generations spanning three stages from early to late: Qz1 (Stage I), Qz2a and Qz2b (Stage II), and Qz3a and Qz3b (Stage III) (Figure 5). The euhedral-subhedral Qz1 crystals (100–600 μm in size) commonly exhibit a distinct dark-gray CL color and is texturally homogeneous (no zoning or replacement textures) (Figures 5A, B). Qz1 crystals commonly coexists with pyrite (Figures 5A, B). Early-formed Qz2a (dark gray) and late-formed Qz2b (light gray) are the two types of Qz2 crystals. With a distinct border between the two, Qz2b (anhedral structure) cuts and/or replaces Qz2a, which mostly occurs as subhedral to anhedral grains, in a vein-like/net-like structure (Figures 5C, D). Qz3 crystals are separated into two types: late-formed Qz3b (light gray) and early-formed Qz3a (gray-black). Anhedral Qz3b typically cuts and/or replaces the subhedral-anhedral Qz3a (Figures 5E, F).

5.2 Trace element geochemistry

A total of 54 LA–ICP–MS spot analyses were completed on the pyrite from each of the five generations—including Qz1

TABLE 1 Descriptions of representative samples at Yanzhupo.

Sample No.	Stage	Mineral assemblages	Orebody No.
ZK3502-12	I	Qz-Ank-Py	I-1
ZK3502-13	I	Qz-Ank-Py	I-1
ZK1001-23	I	Qz-Ank-Py	III
ZK3701-1	I	Qz-Ank-Py	III
ZK3502-40	I, II	Qz-Ank-Py, Qz-Ank-Chl-Py-Ng	I-1
ZK3502-44	II	Qz-Ank-Chl-Py-Ng	I-1
ZK3301-40	II	Qz-Ank-Chl-Py-Ng	I-1
ZK3301-41	II	Qz-Ank-Chl-Py-Ng	II
ZK3901-17	II	Qz-Ank-Chl-Py-Ng	II
ZK3502-45	II, III	Qz-Ank-Chl-Py-Ng, Qz-Ank-Cal-Py	III
ZK1002-36	III	Qz-Ank-Cal-Py	I-1
ZK3701-23	III	Qz-Ank-Cal-Py	I-1
ZK3901-25	III	Qz-Ank-Cal-Py	II

Abbreviations: Qz, quartz; Ank, ankerite; Chl, chlorite; Cal, calcite; Py, pyrite; Ng, native gold.

(n = 10), Qz2a (n = 12), Qz2b (n = 10), Qz3a (n = 11), and Qz3b (n = 11); the trace-element compositions are provided in Supplementary Appendix Table SA1 and illustrated in Figure 6. Qz1 contains the greatest Ti (0.670 ppm–2.96 ppm), Mn (4.96 ppm–40.8 ppm), Fe (25.0 ppm–4,363 ppm), Zn (2.61 ppm–24.5 ppm), and Pb (0.247 ppm–13.9 ppm). Qz2a has the greatest median contents of Li (12.0 ppm–142 ppm), Al (48.8 ppm–3,468 ppm), and Ge (2.02 ppm–11.2 ppm). Qz3a has higher median contents of Na (620 ppm–20,770 ppm), Mg (7.91 ppm–439 ppm), Al (206 ppm–29,329 ppm), and Ti (0.139 ppm–29.4 ppm) but lower median contents of Li (0.520 ppm–23.9 ppm), K (53.5 ppm–1,453 ppm), and Ge (2.56 ppm–2.61 ppm) compared to Qz3b. Furthermore, the concentrations of Li, Al, K, Fe, Zn, Ge, As, Sr, and Sb decrease from Qz2a to Qz2b, whereas the Na, Mg, Ti, Rb, and Pb contents show the opposite trend. The contents of Na, Mg, Al, Ti, Mn, Fe, Cu, Rb, and Pb decrease from Qz3a to Qz3b, whereas other elements show the opposite trend (e.g., Li, K, Ge, Sr, and Sb).

6 Discussions

6.1 Trace element occurrence in quartz

Significant amounts of trace elements, such as Al, B, Ca, Cr, Cu, Fe, Ge, H, K, Li, Mg, Mn, Na, P, Rb, Pb, Ti, and U, were found in quartz in earlier geochemical investigations (Müller et al., 2003; Landtwing and Pattke, 2005; Müller and Koch-Müller, 2009). These elements are usually present in quartz as micro-crystalline inclusions or as replacements within the crystal structure (Jacamon and Larsen, 2009; Rottier and Casanova, 2021). Information on the presence of trace elements in quartz may be obtained via LA–ICP–MS time-resolved signal spectra. The uniform distributions of these elements and their likely presence in the quartz crystal lattice are shown by the flat and steady time-resolved LA–ICP–MS signals of Al, Na, K, Mg, Li, Mn, Fe, Ge, and Ti for Qz1 (Figure 7A). On the other hand, outliers in box-and-whisker plots could represent uniformly distributed nano-inclusions that LA–ICP–MS is unable to resolve (Keith et al., 2022; Zhang et al., 2022). Consequently, the high concentrations (outliers) for Mg in Qz2a, Mg and Al in Qz2b, and Fe in Qz3 (Figure 6) show that the aforementioned elements may be nano-inclusions in these quartz varieties. The local signal maxima of Mg, Al (Figure 7C), and Fe (Figure 7D) likewise show this. In the meanwhile, the broad ranges of Fe concentrations of Qz3 (Figure 6) provide more evidence for the occurrence of micro-inclusion (Zhang et al., 2022).

Additional point defects may arise via the substitution of mono-, tri-, tetra-, and pentavalent cations in the interstitial or tetrahedral locations in the hydrothermal quartz crystal structure, according to earlier research (Rusk 2012; Hong et al., 2024). Three different substitution mechanisms are possible: (1) replacing Si^{4+} cations with trivalent cations (Al^{3+}, Fe^{3+}, Sb^{+}, and As^{3+}) and balancing it with univalent cations (e.g., Li^{+}, Rb^{+}, K^{+}); (2) substituting two Si atoms with a combination of trivalent and pentavalent cations (P^{5+}) to make up for a charge deficit; and (3) directly substituting a Si atom with tetravalent cations (Ti^{4+} and Ge^{4+}) based on the same valence and similar ionic radius (Müller and Koch-Müller, 2009). The concentration of Al exhibits a positive correlation with K (Figure 8A) and alkali metals (Figure 8B) following the removal of geochemical outliers from the quartz samples. This suggests that Si^{4+}

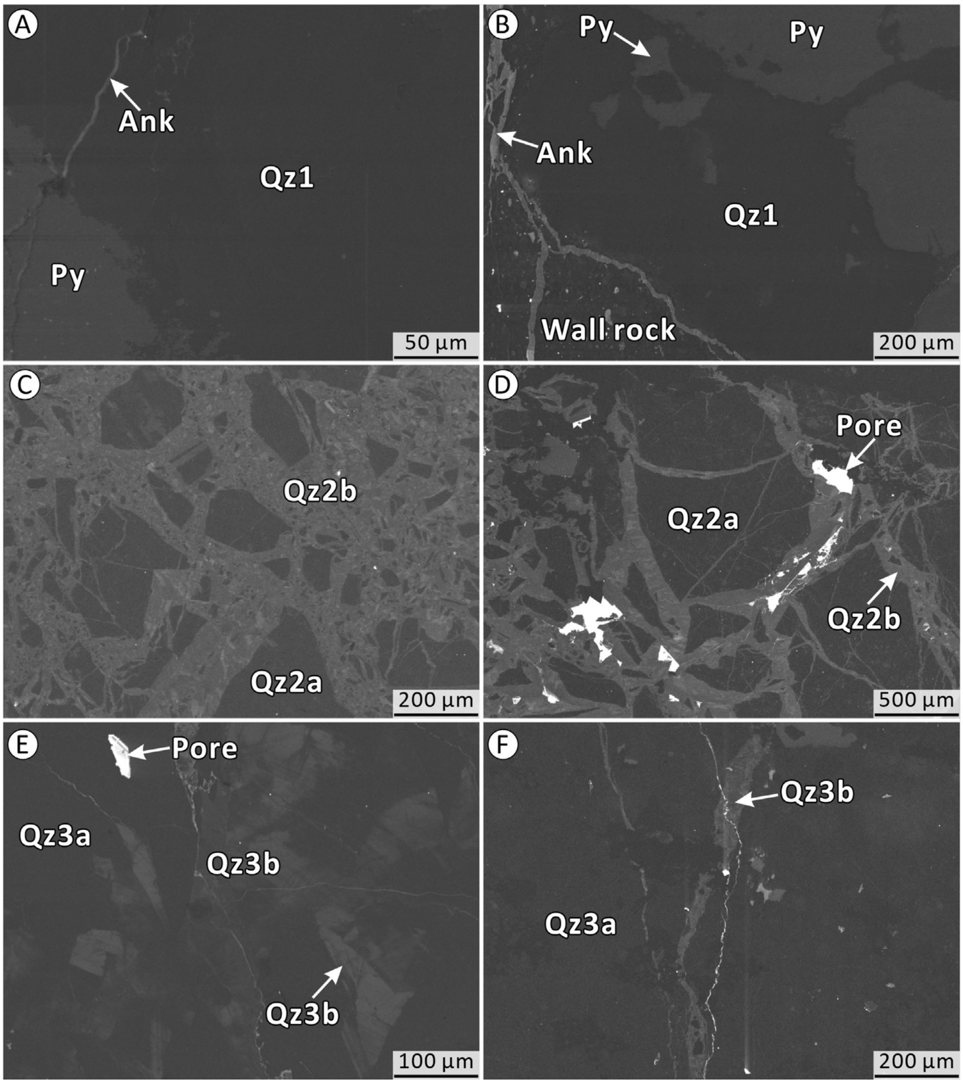

FIGURE 5
Cathodoluminescence (CL) images of quartz from the Yanzhupo deposit: **(A, B)** Qz1 commonly exhibit a distinct dark-gray CL color; **(C, D)** Qz2b (light gray) cuts and/or replaces Qz2a (dark gray); **(E, F)** light-grey Qz3b replaced Qz3a in patches. Abbreviations: Qz, quartz; Py, pyrite; Ank, ankerite.

is replaced by Al^{3+} and charge-compensated univalent cations in the Yanzhupo quartz crystals for all quartz generations (Zhang Y. et al., 2019). However, the substitution of Al^{3+} and Sr^{2+} for Si^{4+} in the three quartz generations at Yanzhupo is not supported by the lack of a link between the quantities of Al and Sr (Figure 8C). In the three quartz generations at Yanzhupo, in Jiangnan Orogen, South China, there is a positive association between Al and Ge, even though Rusk (2012) found no link between Ge and other elements in quartz (Figure 8A). This provides an indication for the discussion of the occurrence state of the Al-Ge element in quartz of similar deposits in the world.

6.2 Physicochemical conditions of the Yanzhupo mineralization

Quartz geochemistry and CL intensity variations in multiple generations of quartz are influenced by the evolving physicochemical conditions of hydrothermal fluids (Zhang Y. et al., 2019; Feng et al., 2020b; Gao et al., 2022; Hong et al., 2024). Research shows that quartz developed through hydrothermal processes at temperatures below 350°C typically has less than 10 ppm Ti contents, whereas quartz formed at temperatures above 400°C normally contains more than 10 ppm (Rusk et al., 2008).

Titanium median concentrations in quartz at Yanzhupo are predominantly below 10 ppm (Qz1: 0.743 ppm; Qz2: 0.315 ppm; Qz3: 0.427 ppm; Figure 6). This indicates fluid temperatures were likely below 350°C. Such temperatures promote quartz precipitation over dissolution. According to Fournier (1983), quartz solubility rises with temperature between 300°C and 450°C. Generally, Ti contents in quartz are directly proportional to its crystallization temperature, thus the variations in Ti concentrations from Qz1 (avg. 0.743 ppm) through Qz2 (avg. Qz2: 0.315 ppm) to Qz3 (avg. 0.427 ppm) indicate an initial drop in temperature followed by a slight rise in temperature during quartz precipitation. Conversely,

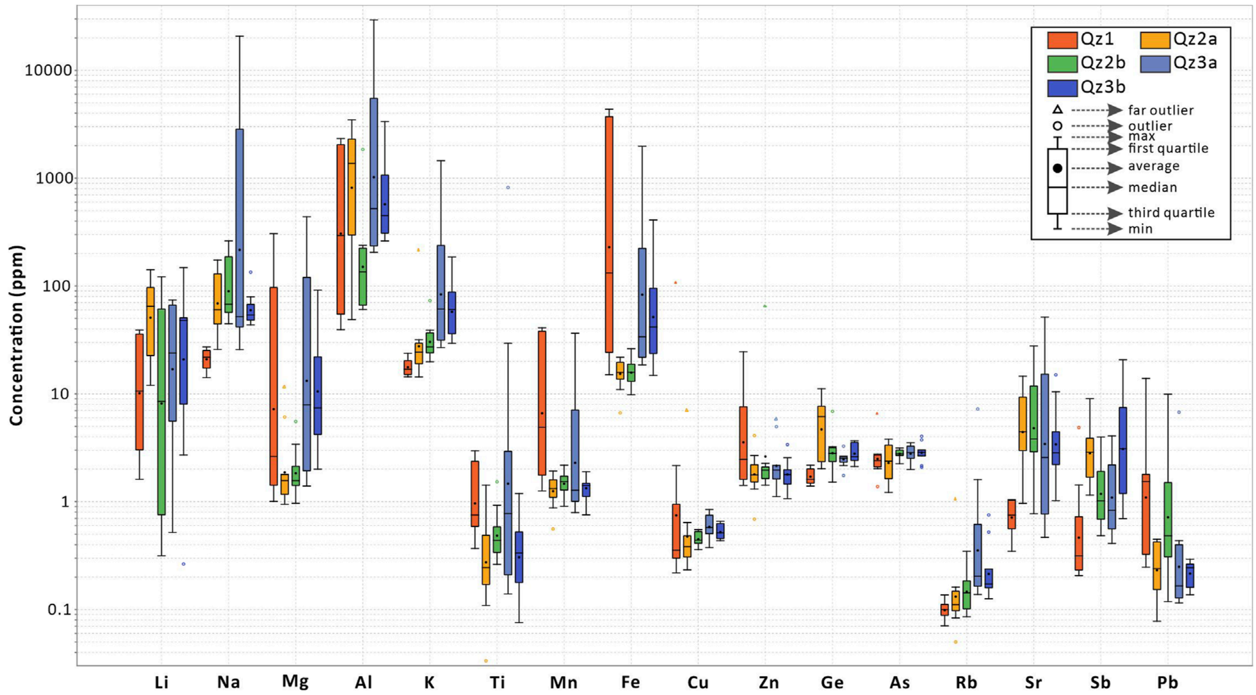

FIGURE 6
Box and whisker plot for trace element contents of the five quartz types from Yanzhupo.

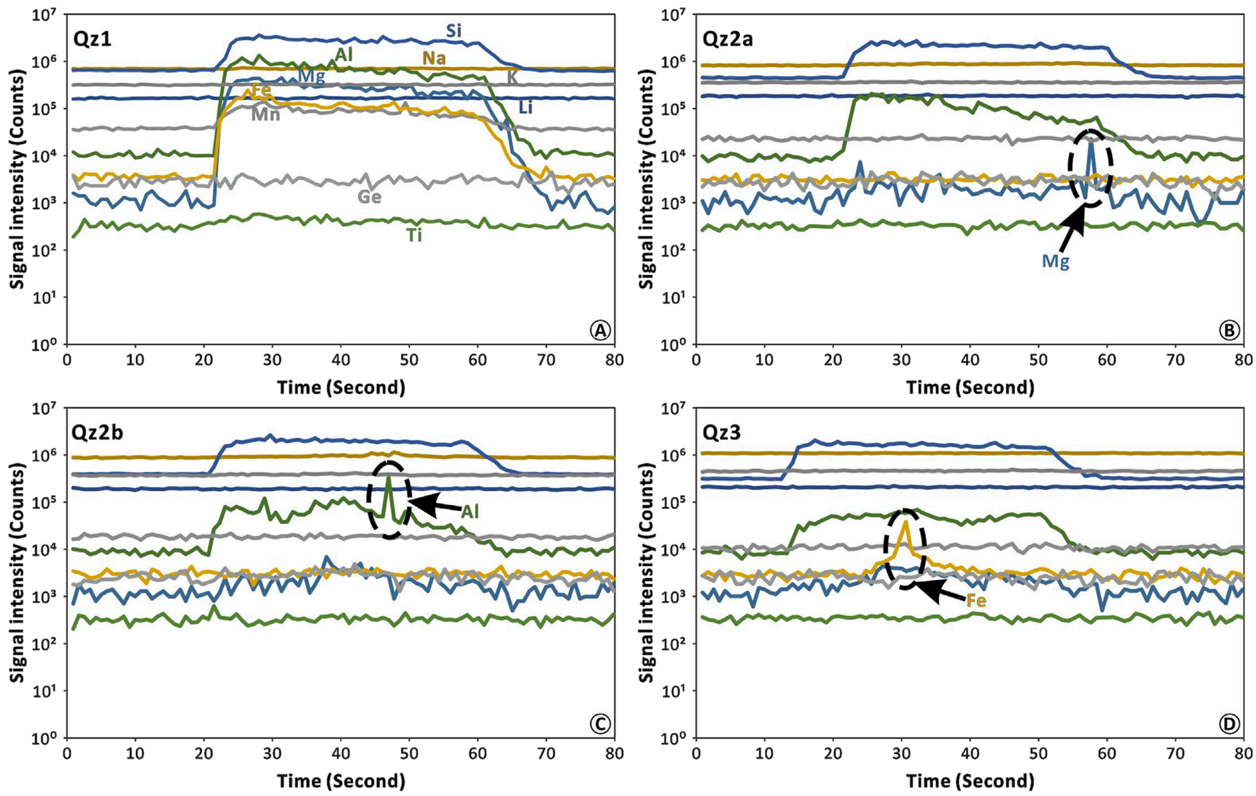

FIGURE 7
Representative LA–ICP–MS time-resolved depth profiles for the Yanzhupo quartz. Abbreviations: Qz, quartz; Al, aluminium; Mg, magnesium; Na, natrium; Li, lithium; K, kalium; Mn, manganese; Fe, iron; Si, silicon; Ti, titanium; Ge, germanium.

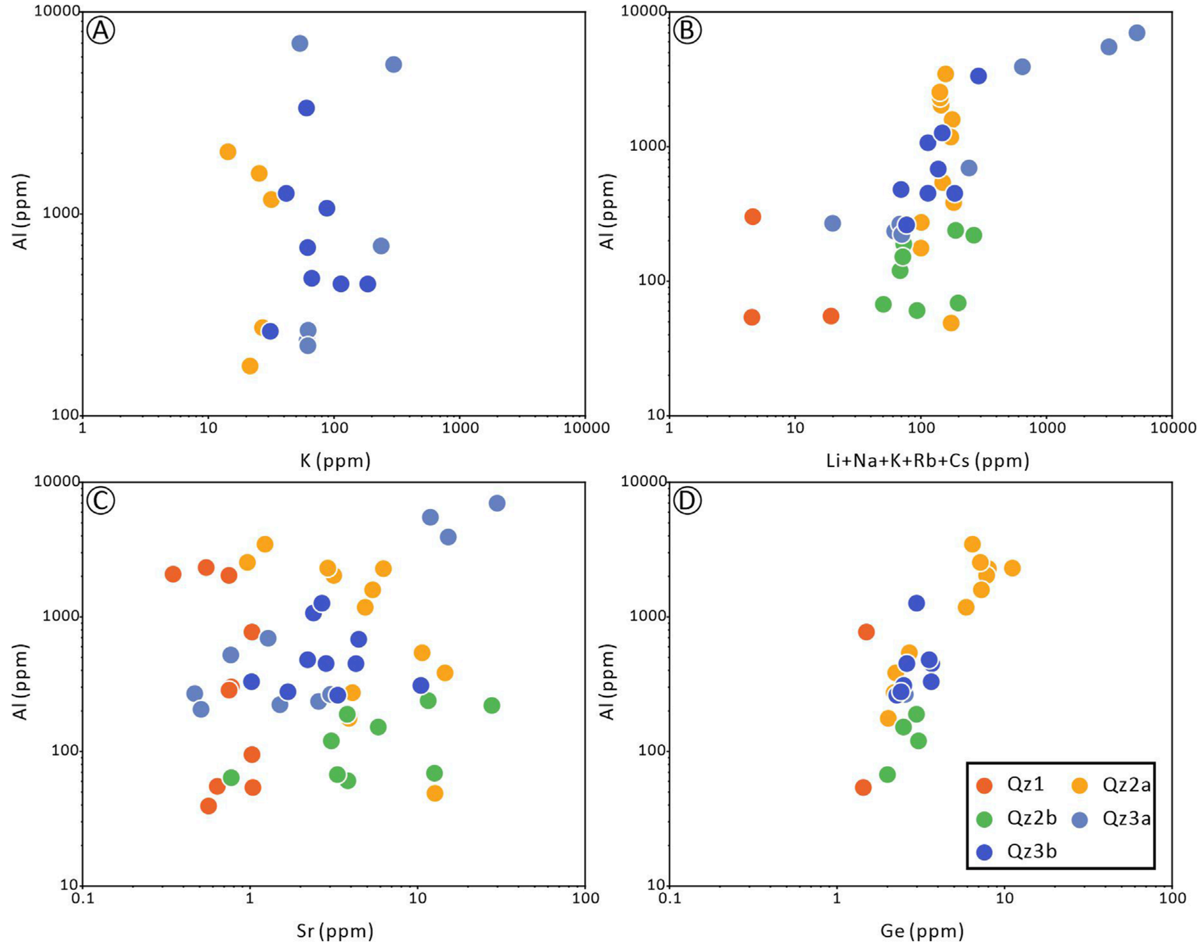

FIGURE 8
Binary plots of **(A)** K vs. Al; **(B)** (Li + Na + K + Rb + Cs) vs. Al; **(C)** Sr vs. Al; **(D)** Ge vs. Al for the Yanzhupo quartz.

Ge/Ti ratios decrease with increasing temperature (Rottier and Casanova, 2021). The average Ge/Ti ratios for Qz1, Qz2, and Qz3 are 0.65, 11.49, and 5.17, respectively, showing a similar temperature trend as revealed by Ti contents. Aluminum, as the predominant trace element found in quartz, can be a reliable indicator of the solubility of Al in ore-forming fluids, which rises as the fluid pH drops (Rusk et al., 2008). Elevated Al levels in quartz may indicate a higher level of fluid acidity in the fluid (Rusk, 2012; Hong et al., 2024). Aluminum concentrations increase from Qz1 (avg. 294 ppm) through Qz2 (avg. 238 ppm) to Qz3 (avg. 465 ppm), indicating initial increase in pH followed by a decrease in pH during the evolution of the system and therefore its fluids (Figure 6).

According to the afore-discussed temperature and pH evolution, Qz1 is Ti-rich, Al-depleted (Figure 6), suggestive of high temperature and pH during the formation of Qz1. The subsequent temperature and encouraged Qz2a to form. However, the sudden decrease in Al content from Qz2a to Qz2b (Figure 6) indicates that it was formed at high pH, coupled with the closely related relationship between Qz2b and native gold (Figure 4G), which may be associated with an intensive water-rock reaction, which may have led to the Stage II Au precipitation.

6.3 Ore genesis and metallogenic implications

Gold deposits in the Jiangnan Orogen were variably attributed to be SEDEX (Gu et al., 2007; Gu et al., 2012), epithermal (Ye et al., 1994), orogenic (Goldfarb et al., 2001; Ni et al., 2015), or intrusion-related (Yang et al., 2013; Wen et al., 2016). For the Yanzhupo Au deposit, a SEDEX-type origin can be excluded since the mineralization is mostly vein-type that crosscut the sandstone slate of the Leishenmiao Formation in the Lengjiaxi Group with sharp contact (Figure 2B).

Some previous studies have used the Al-Ti contents in quartz to fingerprint the gold deposit types (Rusk, 2012; Zhang Y. et al., 2019; Feng et al., 2020b; Yan et al., 2020). For the Yanzhupo quartz samples, their Al contents (39.3–29,329 ppm) are obviously higher than those from typical orogenic gold deposits (100–1,000 ppm) (Rusk, 2012), suggesting that orogenic-type origin is also unlikely. Titanium contents (0.076–29.4 ppm) of the Yanzhupo quartz fall mainly outside the range of typical porphyry deposits (>3 ppm) (Rusk et al., 2008; Rusk 2012). In the Al–Ti diagram (Figure 9), the Yanzhupo quartz distinctly differs from porphyry and orogenic Au deposits, but overlaps with epithermal Au deposits, indicating a magmatic-hydrothermal origin of Au mineralization. This is consistent with the

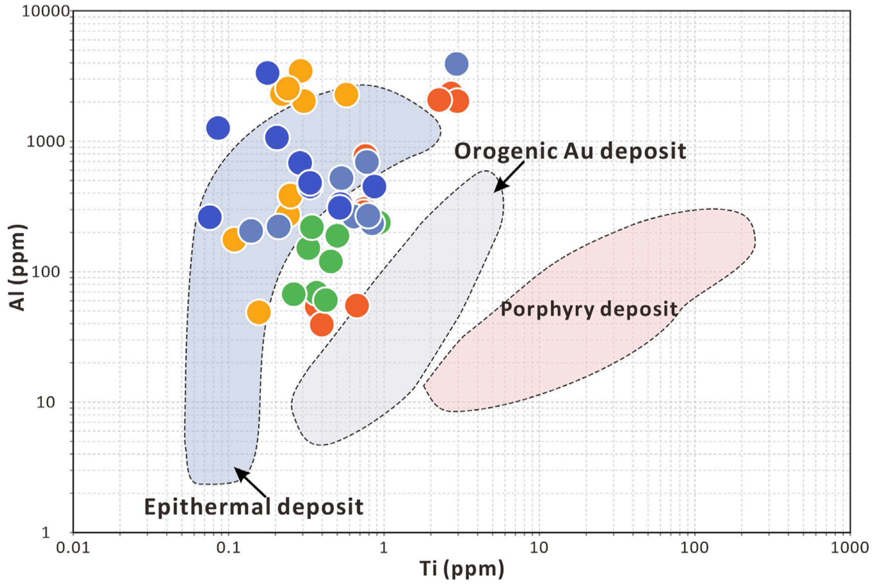

FIGURE 9
Discrimination graphs of Al vs. Ti contents in the different types of deposits. The background color fields come from Rusk (2012).

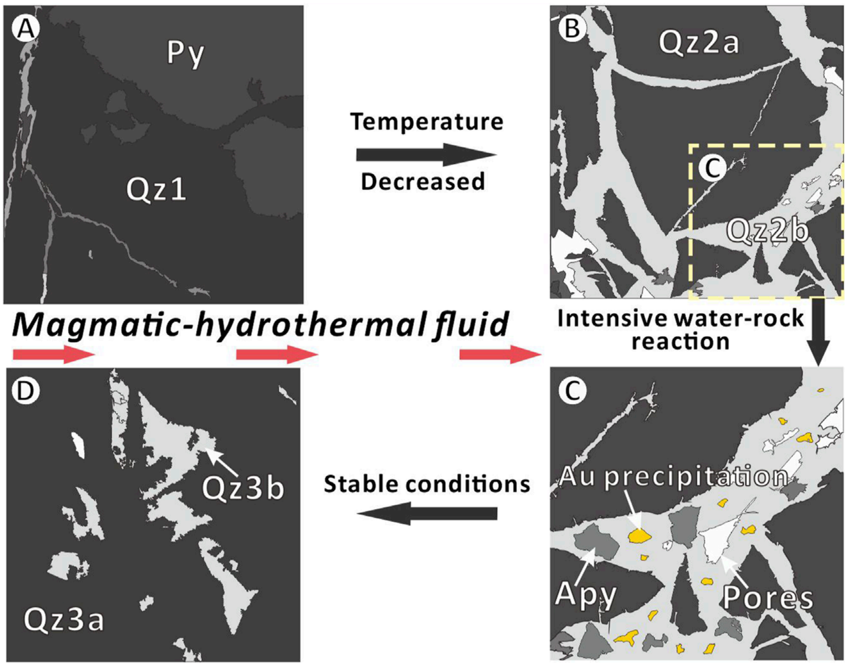

FIGURE 10
Schematic diagram for the ore formation at Yanzhupo. See text for details. Abbreviations: Qz, quartz; Apy, arsenopyrite; Au, gold; Py, pyrite.

magmatic-hydrothermal ore features (Figure 2B), and magmatic-hydrothermal ore mineral assemblage (incl. Sphalerite, galena, pyrite, arsenopyrite, and chalcopyrite) (Figure 4).

Accordingly, we propose the following metallogenic process for the Yanzhupo deposit (Figure 10):

The magma-derived hydrothermal fluids percolated along the fault (Figure 10A), and entered the sandstone slate of the Leishenmiao Formation in the Lengjiaxi Group. The fluid deposited Qz1 via high temperature and pH values (Figure 10A). With the continuous ore-fluid injection, the gradual decrease in temperature gradually encouraged Qz2a to form (Figure 10B). Subsequently, the ore-fluid deposited Qz2b via intensive water-rock interaction, which may have induced the Stage II Au precipitation (Figure 10C). Finally, the sealing of fractures by veins may have caused the formation of Qz3 under stable conditions (Figure 10D).

7 Conclusion

(1) The Yanzhupo mineralization can be divided into three stages (I) pre-ore quartz-ankerite-pyrite, (II) main-ore quartz-ankerite-chlorite-pyrite-gold, and (III) late ore quartz-ankerite-calcite-pyrite.
(2) The hydrothermal quartz at Yanzhupo can be categorized five generations: texturally homogeneous Qz1, the homogeneous Qz2a and the younger Qz2b that cut Qz2a, and, texturally homogeneous Qz3a and the younger Qz3b that replaced Qz3a.
(3) The main trace elements incorporated into Yanzhupo quartz generations include trivalent Al^{3+}, which is coupled with monovalent alkali metals (Li^{+}, Na^{+}, K^{+}, Rb^{+}, and Cs^{+}) and bivalent cations (Ge^{2+}) substituting for Si^{4+}.
(4) The sudden increase in Al concentrations from Qz2a to Qz2b indicates that it was formed under high pH conditions, likely due to intense water-rock interaction, which facilitated the precipitation of gold in Stage II at Yanzhupo.
(5) The Yanzhupo Au deposit exhibits Al and Ti concentrations as well as Al/Ti ratios comparable to those in magmatic-hydrothermal deposits. Additionally, it displays characteristics typical of magmatic-hydrothermal ores, including mineral assemblages such as sphalerite, galena, pyrite, arsenopyrite, and chalcopyrite. This evidence suggests that the deposit is likely of magmatic-hydrothermal origin.

Data availability statement

The original contributions presented in the study are included in the article/Supplementary Material, further inquiries can be directed to the corresponding author.

Author contributions

NP: Conceptualization, Data curation, Funding acquisition, Investigation, Project administration, Supervision, Validation, Writing–original draft, Writing–review and editing. HS: Data curation, Formal Analysis, Methodology, Visualization, Writing–original draft, Writing–review and editing. JL: Formal Analysis, Investigation, Methodology, Resources, Software, Validation, Visualization, Writing–review and editing.

Funding

The author(s) declare financial support was received for the research, authorship and/or publication of this article. This research was funded by the Geological Survey Projects of the China Geological Survey (DD20220969).

Acknowledgments

Special thanks are given to Mr. Yiwei Zhu for helping with the fs–LA–ICP–MS trace element analysis.

Conflict of interest

The authors declare that the research was conducted in the absence of any commercial or financial relationships that could be construed as a potential conflict of interest.

The reviewer WS declared a shared affiliation with the author HS to the handling editor at time of review.

Generative AI statement

The author(s) declare that no Generative AI was used in the creation of this manuscript.

Supplementary material

The Supplementary Material for this article can be found online at: https://www.frontiersin.org/articles/10.3389/feart.2025.1566088/full#supplementary-material

References

Cawood, P. A., Wang, Y., Xu, Y., and Zhao, G. (2013). Locating South China in rodinia and gondwana: a fragment of greater India lithosphere? *Geology* 41, 903–906. doi:10.1130/g34395.1

China Geological Survey. (2024). *Research on the metallogenic mechanism and exploration demonstration of gold deposits in the Xuefeng arc tectonic belt* (in Chinese with English abstract).

Chu, Y., Lin, W., Faure, M., Wang, Q., and Ji, W. (2012). Phanerozoic tectonothermal events of the Xuefengshan Belt, central South China: implications from U-Pb age and Lu-Hf determinations of granites. *Lithos* 150, 243–255. doi:10.1016/j.lithos.2012.04.005

Deng, T., Xu, D., Chi, G., Wang, Z., Chen, G., Zhou, Y., et al. (2020). Caledonian (Early Paleozoic) veins overprinted by Yanshanian (Late Mesozoic) gold mineralization in the Jiangnan Orogen: a case study on gold deposits in northeastern Hunan. South China. *Ore Geol. Rev.* 124, 103586. doi:10.1016/j.oregeorev.2020.103586

Deng, T., Xu, D. R., Chi, G. X., Wang, Z. L., Jiao, Q. Q., Ning, J., et al. (2017). Geology, geochronology, geochemistry, and ore genesis of the Wangu gold deposit in northeastern Hunan Province, Jiangnan Orogen. South China. *Ore Geol. Rev.* 88, 619–637. doi:10.1016/j.oregeorev.2017.01.012

Faure, M., Shu, L., Wang, B., Charvet, J., Choulet, F., and Monie, P. (2009). Intracontinental subduction: a possible mechanism for the early palaeozoic orogen of SE China. *Terra nova.* 21, 360–368. doi:10.1111/j.1365-3121.2009.00888.x

Feng, Y., Zhang, Y. u., Xie, Y., Shao, Y., and Lai, C. (2020a). Pyrite geochemistry and metallogenic implications of Gutaishan Au deposit in Jiangnan Orogen. South China. *Ore Geol. Rev.* 117, 103298. doi:10.1016/j.oregeorev.2019.103298

Feng, Y., Zhang, Y. u., Xie, Y., Shao, Y., Tan, H., Li, H., et al. (2020b). Ore-forming mechanism and physicochemical evolution of Gutaishan Au deposit, South China: perspective from quartz geochemistry and fluid inclusions. *Ore Geol. Rev.* 119, 103382. doi:10.1016/j.oregeorev.2020.103382

Fournier, R. B. (1983). A method of calculating quartz solubilities in aqueous sodium chloride solutions. *Geochim. Cosmochim. AC* 47, 579–586. doi:10.1016/0016-7037(83)90279-x

Gao, L., Guo, J. L., Chen, X. G., Chen, J. H., Liu, Y., Wang, J. Y., et al. (2019). An over-view of timing and structural geometry of gold, gold-antimony and antimony mineralization in the Jiangnan orogen, southern China. *Ore Geol. Rev.* 115, 103173. doi:10.1016/j.oregeorev.2019.103173

Gao, S., Zhou, X. Z. Y., Hofstra, A. H., Qin, K. Z., Marsh, E. E., Bennett, M. M., et al. (2022). Trace elements in quartz: insights into source and fluid evolution in magmatic-hydrothermal systems. *Econ. Geol.* 117, 1415–1428. doi:10.5382/econgeo.4943

Goldfarb, R. J., Groves, D. I., and Gardoll, S. (2001). Orogenic gold and geologic time: a global synthesis. *Ore Geol. Rev.* 18, 1–75. doi:10.1016/s0169-1368(01)00016-6

Gu, X., Schulz, O., Vavtar, F., Liu, J., Zheng, M., and Fu, S. (2007). Rare earth element geochemistry of the Woxi W-Sb–Au deposit, Hunan province, South China. *Ore Geol. Rev.* 31, 319–336. doi:10.1016/j.oregeorev.2005.01.003

Gu, X., Zhang, Y., Schulz, O., Vavtar, F., Liu, J., Zheng, M., et al. (2012). The Woxi W-Sb–Au deposit in Hunan, South China: an example of Late Proterozoic sedimentary exhalative (SEDEX) mineralization. *J. Asian Earth Sci.* 57, 54–75. doi:10.1016/j.jseaes.2012.06.006

Han, F. B., Chang, L., Cai, M. H., Liu, S. Y., Zhang, S. Q., Chen, Y., et al. (2010). Ore-forming epoch of gold deposits in northeastern Hunan. *Mineral. Deposits* 29, 563–571. (in Chinese with English abstract). doi:10.3969/j.issn.0258-7106.2010.03.017

Hong, J. X., Zhai, D. G., and Keith, M. (2024). Quartz texture and the chemical composition fingerprint of ore-forming fluid evolution at the Bilihe porphyry Au deposit, NE China. *Am. Mineral.* 109, 1203–1219. doi:10.2138/am-2022-8840

Jacamon, F., and Larsen, R. B. (2009). Trace element evolution of quartz in the charnockitic Kleivan granite, SW-Norway: the Ge/Ti ratio of quartz as an index of igneous differentiation. *Lithos* 107, 281–291. doi:10.1016/j.lithos.2008.10.016

Ji, W., Chen, Y., Chen, K., Wei, W., Faure, M., and Lin, W. (2018). Multiple emplacement and exhumation history of the late Mesozoic Dayunshan-Mufushan batholith in southeast China and its tectonic significance: 1. Structural analysis and geochronological constraints. *J. Geophys. Res. Solid Earth.* 123, 689–710. doi:10.1002/2017jb014597

Jia, S. S., Wang, E. D., Fu, J. F., Wang, X. D., and Li, W. Q. (2019). Geology, fluid inclusions and isotope geochemistry of the Herenping gold deposit in the southern margin of the Yangtze Craton, China: a sediment-hosted reduced intrusion-related gold deposit? *Ore Geol. Rev.* 107, 926–943. doi:10.1016/j.oregeorev.2019.03.031

Keith, M., Haase, K. M., Chivas, A. R., and Klemd, R. (2022). Phase separation and fluid mixing revealed by trace element signatures in pyrite from porphyry systems. *Geochim. Cosmochim. AC* 329, 185–205. doi:10.1016/j.gca.2022.05.015

Landtwing, M. R., and Pettke, T. (2005). Relationships between SEM-cathodoluminescence response and trace-element composition of hydrothermal vein quartz. *Am. Mineral.* 90, 122–131. doi:10.2138/am.2005.1548

Li, H., Danišík, M., Zhou, Z. K., Jiang, W. C., and Wu, J. H. (2020). Integrated U–Pb, Lu–Hf and (U–Th)/He analysis of zircon from the Banxi Sb deposit and its implications for the low-temperature mineralization in South China. *Geosci. Front.* 11, 1323–1335. doi:10.1016/j.gsf.2020.01.004

Li, H., Zhu, D. P., Shen, L. W., Algeo, T. J., and Elatikpo, S. M. (2022). A general ore formation model for metasediment-hosted Sb-(Au-W) mineralization of the Woxi and Banxi deposits in South China. *Chem. Geol.* 607, 121020. doi:10.1016/j.chemgeo.2022.121020

Li, J. H., Dong, S. W., Zhang, Y. Q., Zhao, G. C., Johnston, S. T., Cui, J. J., et al. (2016). New insights into Phanerozoic tectonics of south China: Part 1, polyphase deformation in the Jiuling and Lianyunshan domains of the central Jiangnan orogen. *J. Geophys. Res. Solid Earth.* 121, 3048–3080. doi:10.1002/2015jb012778

Li, J. H., Zhang, Y. Q., Dong, S. W., Ma, Z. L., and Li, Y. (2015). LA-MC-ICPMS zircon U-Pb geochronology of the Hongxiaqiao and Banshanpu granitoids in eastern hunan province and its geological implications. *Acta Geol. Sin.* 36, 187–196. (in Chinese with English abstract). doi:10.3975/cagsb.2015.02.07

Li, P., Xu, D., Chen, G., Xia, B., He, Z., and Fu, G. (2005). Constraints of petrography, geochemistry and Sr–Nd isotopes on the Jinjing granitoids from northeastern Hunan province, China: implications for petrogenesis and geodynamic setting. *Acta Petrol. Sin.* 21, 921–934. (in Chinese with English abstract). doi:10.3969/j.issn.1000-0569.2005.03.030

Li, W., Cook, N. J., Xie, G. Q., Mao, J. W., Ciobanu, C. L., and Fu, B. (2021). Complementary textural, trace element, and isotopic analyses of sulfides constrain ore-forming processes for the slate-hosted yuhengtang Au deposit. South China. *Econ. Geol.* 116 (8), 1825–1848. doi:10.5382/econgeo.4847

Li, W., Cook, N. J., Xie, G.-Q., Mao, J. W., Ciobanu, C. L., Li, J. W., et al. (2019). Textures and trace element signatures of pyrite and arsenopyrite from the Gutaishan Au–Sb deposit. South China. *Min. Deposita* 54 (4), 591–610. doi:10.1007/s00126-018-0826-0

Li, X., Li, Z., Ge, W., Zhou, H., Li, W., Liu, Y., et al. (2003). Neoproterozoic granitoids in South China: crustal melting above a mantle plume at ca. 825 Ma? *Precambr. Res.* 122, 45–83. doi:10.1016/S0301-9268(02)00207-3

Liao, J., Wang, X., Chen, B., Wang, B. Q., Zhu, Z. H., Wang, W. T., et al. (2025). Pyrite textures, trace element geochemistry and galena Pb iso-topes of the Yanzhupo gold deposit in the jiangnan orogen, south China: implications for gold mineralization genesis. *Minerals* 15, 94. doi:10.3390/min15010094

Liu, Q. Q., Shao, Y. J., Chen, M., Thomas, J. A., Li, H., Jeffrey, M. D., et al. (2019). Insights into the genesis of orogenic gold deposits from the Zhengchong goldfield, northeastern Hunan Province, China. *Ore Geol. Rev.* 105, 337–355. doi:10.1016/j.oregeorev.2019.01.002

Lu, W., Sun, J., Zhou, C., Guo, A. M., and Peng, W. (2020). A study of the source of metallogenic material and characteristics of the ore-forming fluid in the Yanlinsi gold deposit in northeastern Hunan Province. *Acta Geol. Sin.* 41, 384–394. (in Chinese with English abstract). doi:10.3975/cagsb.2020.032301

Madayipu, N., Li, H., Algeo, T. J., Elatikpoa, S. M., Heritier, R. N., Zhou, H. X., et al. (2023b). Long-lived Nb-Ta mineralization in mufushan, NE hunan, south China: geological, geochemical, and geochronological constraints. *Geosci. Front.* 14, 101491. doi:10.1016/j.gsf.2022.101491

Madayipu, N., Li, H., Elatikpo, S. M., Ghaderi, M., Heritier, R. N., Hu, X. J., et al. (2024). Tracing fluid exsolution and hydrothermal alteration signature of the Mufushan Nb-Ta-(Li-Be-Cs) deposit, South China: an apatite perspective. *J. Geol. Soc.* 181, jgs2023–087. doi:10.1144/jgs2023-087

Madayipu, N., Li, H., Elatikpoa, S. M., Förster, M. W., Zhou, H. X., Zheng, H., et al. (2023a). Magmatic-hydrothermal evolution of long-lived Nb-Ta-(Sn) mineralization in lianyunshan, NE hunan, south China. *Geol. Soc. Am. Bull.* 135, 2691–2709. doi:10.1130/B36591.1

Müller, A., Herklotz, G., and Giegling, H. (2018). Chemistry of quartz related to the Zinnwald/Cínovec Sn-W-Li greisen-type deposit, Eastern Erzgebirge, Germany. *J. Geochem. Explor.* 190, 357–373. doi:10.1016/j.gexplo.2018.04.009

Müller, A., Herrington, R., Armstrong, R., Seltmann, R., Kirwin, D. J., Stenina, N. G., et al. (2010). Trace elements and cathodoluminescence of quartz in stockwork veins of Mongolian porphyry-style deposits. *Min. Deposita* 45, 707–727. doi:10.1007/s00126-010-0302-y

Müller, A., and Koch-Müller, M. (2009). Hydrogen speciation and trace element contents of igneous, hydrothermal and metamorphic quartz from Norway. *Mineral. Mag.* 73, 569–583. doi:10.1180/minmag.2009.073.4.569

Müller, A., Wiedenbfexk, M., Van Den Kerkhof, A. M., Kronz, A., and Simon, K. (2003). Trace elements in quartz – a combined electron microprobe, secondary ion mass spectro-metry, laser-ablation ICP-MS, and cathodoluminescence study. *Eur. J. Mineral.* 15, 747–763. doi:10.1127/0935-1221/2003/0015-0747

Ni, P., Wang, G. G., Chen, H., Xu, Y. F., Guan, S. J., Pan, J. Y., et al. (2015). An Early Paleozoic orogenic gold belt along the Jiangshao Fault, South China: evidence from fluid inclusions and Rb-Sr dating of quartz in the Huangshan and Pingshui deposits. *J. Asian Earth Sci.* 103, 87–102. doi:10.1016/j.jseaes.2014.11.031

Qiu, K. F., Deng, J., Yu, H. C., Wu, M. Q., Wang, Y., Zhang, L., et al. (2021). Identifying hydrothermal quartz vein generations in the Taiyangshan porphyry Cu-Mo deposit (West Qinling, China) using cathodoluminescence, trace element geochemistry, and fluid inclusions. *Ore Geol. Rev.* 128, 103882. doi:10.1016/j.oregeorev.2020.103882

Qiu, X. Y., Li, W. B., Zhang, L. J., Zhang, F. H., Zhu, X. F., and Xia, X. P. (2022). Textural, fluid inclusion, and *in-situ* oxygen isotope studies of quartz: constraints on vein formation, disequilibrium fractionation, and gold precipitation at the Bilihe gold deposit, Inner Mongolia, China. *Am. Mineral.* 107, 517–531. doi:10.2138/am-2021-7823

Rottier, B., and Casanova, C. (2021). Trace element composition of quartz from porphyry systems: a tracer of the mineralizing fluid evolution. *Min. Deposita* 56, 843–862. doi:10.1007/s00126-020-01009-0

Rusk, B. (2012). "Cathodoluminescent textures and trace elements in hydrothermal quartz," in *Quartz: deposits, mineralogy and analytics*. Editors J. Götze, and R. Möckel (Berlin: Springer Geology, Springer), 307–329.

Rusk, B. G., Lowers, H. A., and Reed, M. H. (2008). Trace elements in hydrothermal quartz: relationships to cathodoluminescent textures and insights into vein formation. *Geology* 36, 547–550. doi:10.1130/g24580a.1

Shu, L. S., Yao, J. L., Wang, B., Faure, M., Charvet, J., and Chen, Y. (2021). Neoproterozoic plate tectonic process and Phanerozoic geodynamic evolution of the South China Block. *Earth Sci. Rev.* 216, 103596. doi:10.1016/j.earscirev.2021.103596

Tan, H. J., Shao, Y. J., Liu, Q. Q., Zhang, Y., Feng, Y. Z., Zhang, Y. C., et al. (2022). Textures, trace element geochemistry and *in-situ* sulfur isotopes of pyrite from the Xiaojiashan gold deposit, Jiangnan Orogen: implications for ore genesis. *Ore Geol. Rev.* 144, 104843. doi:10.1016/j.oregeorev.2022.104843

Tanner, D., Henley, R. W., Mavrogenes, J. A., and Holden, P. (2013). Combining *in situ* isotopic, trace element and textural analyses of quartz from four magmatic-hydrothermal ore deposits. *Contrib. Mineral. Petrol.* 166, 1119–1142. doi:10.1007/s00410-013-0912-3

Wang, C., Shao, Y. J., Evans, N. J., Li, H., Zhou, H. D., Huang, K. X., et al. (2020b). Genesis of zixi gold deposit in xuefengshan, jiangnan orogen (south China): age, geology and isotopic constraints. *Ore Geol. Rev.* 117, 103301. doi:10.1016/j.oregeorev.2019.103301

Wang, C., Shao, Y. J., Goldfarb, R., Tan, S. M., Sun, J., Zhou, C., et al. (2024). Superimposed gold mineralization events in the tuanshanbei orogenic gold deposit, central jiangnan orogen, south China. *South China. Econ. Geol.* 119, 113–137. doi:10.5382/econgeo.5034

Wang, C., Shao, Y. J., Zhang, X., Lai, C. K., Liu, Z. F., Li, H., et al. (2020a). Metallogenesis of the hengjiangchong gold deposit in jiangnan orogen, south China. *Ore Geol. Rev.* 118, 103350. doi:10.1016/j.oregeorev.2020.103350

Wang, D., and Shu, L. (2012). Late Mesozoic basin and range tectonics and related magmatism in Southeast China. *Geosci. Front.* 3, 109–124. doi:10.1016/j.gsf.2011.11.007

Wang, J. Q., Shu, L. S., and Santosh, M. (2016). Petrogenesis and tectonic evolution of Lianyunshan complex, south China: insights on Neoproterozoic and late Mesozoic tectonic evolution of the central Jiangnan Orogen. *Gondwana Res.* 39, 114–130. doi:10.1016/j.gr.2016.06.015

Wang, L., Ma, C., Zhang, C., Zhang, J., and Marks, M. A. (2014). Genesis of leucogranite by prolonged fractional crystallization: a case study of the Mufushan complex South China. *Lithos* 206, 147–163. doi:10.1016/j.lithos.2014.07.026

Wang, Y., Zhang, Y., Fan, W., and Peng, T. (2005). Structural signatures and $^{40}Ar/^{39}Ar$ geochronology of the indosinian xuefengshan tectonic belt, south China block. *J. Struct. Geol.* 27 (6), 985–998. doi:10.1016/j.jsg.2005.04.004

Wen, Z., Deng, T., Dong, G., Zou, F., Xu, D., Wang, Z., et al. (2016). Study on the characters and rules of the ore-controlling structures of the Wangu gold deposit in northeastern Hunan Province. *Geotect. Metallogenia* 40, 1–14. (in Chinese with English abstract). doi:10.16539/j.ddgzyckx.2016.02.007

Wertich, V., Leichmann, J., Dosbaba, M., and Götze, J. (2018). Multi-stage evolution of gold-bearing hydrothermal quartz veins at the Mokrsko gold deposit (Czech Republic) based on cathodoluminescence, spectroscopic, and trace elements analyses. *Minerals* 8, 335. doi:10.3390/min8080335

Xiong, Y. Q., Shao, Y. J., Cheng, Y. B., and Jiang, S. Y. (2020). Discrete jurassic and cretaceous mineralization events at the Xiangdong W(Sn) Deposit, Nanling Range, South China. *Econ. Geol.* 115, 385–413. doi:10.5382/econgeo.4704

Xu, D., Deng, T., Chi, G., Wang, Z., Zou, F., Zhang, J., et al. (2017a). Gold mineralization in the Jiangnan orogenic belt of South China: geological, geochemical and geochronological characteristics, ore deposit-type and geodynamic setting. *Ore Geol. Rev.* 88, 565–618. doi:10.1016/j.oregeorev.2017.02.004

Xu, D. R., Zou, F. H., Ning, J. T., Deng, T., Wang, Z. L., Chen, G. W., et al. (2017b). Discussion on geological and structural characteristics and associated metallogeny in northeastern Hunan Province, South China. *Acta Petrol. Sin.* 33, 695–715. (in Chinese with English abstract).

Yan, C. L., Shu, L. S., Santosh, M., Yao, J. L., Li, J. Y., and Li, C. (2015). The Precambrian tectonic evolution of the western Jiangnan Orogen and western Cathaysia Block: evidence from detrital zircon age spectra and geochemistry of clastic rocks. *Precambrian Res.* 268, 33–60. doi:10.1016/j.precamres.2015.07.002

Yan, J., Mavrogenes, J. A., Liu, S., and Coulson, I. M. (2020). Fluid properties and origins of the Lannigou Carlin-type gold deposit, SW China: evidence from SHRIMP oxygen isotopes and LA-ICP-MS trace element compositions of hydrothermal quartz. *J. Geochem. Explor.* 215, 106546. doi:10.1016/j.gexplo.2020.106546

Yang, J. H., Wang, L., Zhang, J. D., and Yang, S. F. (2013). Characteristics of gravity and magnetic anomalies and gold anomalies in southeast Guizhou and their ore prospecting significance. *Geophys. Geochem. Expor.* 37 (5), 794–799. (in Chinese with English abstract). doi:10.11720/j.issn.1000-8918.2013.5.0

Yao, J. L., Cawood, P. A., Shu, L. S., and Zhao, G. C. (2019). Jiangnan orogen, south China: a ~970–820 Ma rodinia margin accretionary belt. *Earth Sci. Rev.* 196, 102872. doi:10.1016/j.earscirev.2019.05.016

Ye, G. S., Ye, Y. Z., Zhao, G. L., and Bo, Q. R. (1994). Fluid inclusion features of gold (silver) deposit hosted in ductile shear zone in Huangshan region. Zhejiang Province. *Geoscience* 8 (3), 291–298. (in Chinese with English abstract). Available at: https://www.geoscience.net.cn/CN/Y1994/V8/I3/291.

Yuan, M. W., Li, L., Alam, M., Santosh, M., Li, S. R., and Hou, Z. Q. (2023). Correlations between cathodoluminescence intensity and aluminum concentration in low-temperature hydrothermal quartz. *Am. Mineral.* 108, 1224–1231. doi:10.2138/am-2022-8471

Zhang, L., Yang, L. Q., Groves, D. I., Sun, S. C., Liu, Y., Wang, J. Y., et al. (2019b). An over-view of timing and structural geometry of gold, gold-antimony and antimony mineralization in the Jiangnan orogen, southern China. *Ore Geol. Rev.* 115, 103173. doi:10.1016/j.oregeorev.2019.103173

Zhang, Y., Chen, H. Y., Chen, J. M., Tian, J., Zhang, L. J., and Olin, P. (2022). Pyrite geochemistry and its implications on Au-Cu skarn metallogeny: an example from the Jiguanzui deposit, Eastern China. *Am. Mineral.* 107, 1910–1925. doi:10.2138/am-2022-8118

Zhang, Y., Cheng, J. M., Tian, J., Pan, J., Sun, S. Q., Zhang, L. J., et al. (2019a). Texture and trace element geochemistry of quartz in skarn system: perspective from Jiguanzui Cu–Au skarn deposit, Eastern China. *Ore Geol. Rev.* 109, 535–544. doi:10.1016/j.oregeorev.2019.05.007

Zhang, Y. Q., Dong, S. W., Li, J. H., Cui, J. J., Shi, W., Su, J. B., et al. (2012). The new progress in the study of mesozoic tectonics of South China. *Acta Geol. Sin.* 33 (3), 257–279. (in Chinese with English abstract). doi:10.3975/cagsb.2012.03.01

Zhao, C., Ni, P., Wang, G. G., Ding, J. Y., Chen, H., Zhao, K. D., et al. (2013). Geology, fluid inclusion, and isotope constraints on ore genesis of the Neoproterozoic Jinshan orogenic gold deposit, South China. *GEOFLUIDS* 13, 506–527. doi:10.1111/gfl.12052

Zhou, Y. Q., Xu, D. R., Dong, G. J., Chi, G. X., Deng, T., Cai, J. X., et al. (2021). The role of structural reactivation for gold mineralization in northeastern Hunan Province. South China. *J. Struct. Geol.* 145, 104306. doi:10.1016/j.jsg.2021.104306

Zhou, Y. Q., Xu, D. R., Dong, G. J., Wang, Z. L., Cai, J. X., Yan, Z. Q., et al. (2019). Structural evolution of the Changsha-Pingjiang fault zone and its controlling on mineralization. *J. East China Univ. Technol.* 42, 201–208. (in Chinese with English abstract). doi:10.3969/j.issn.1674-3504.2019.03.001